Sculpting the plasmonic responses of nanoparticles by directed electron beam irradiation

Kevin M. Roccapriore, Shin-Hum Cho, Andrew R. Lupini, Delia J. Milliron, and Sergei V. Kalinin**

Dr. Kevin M. Roccapriore, Dr. Andrew R. Lupini, Dr. Sergei V. Kalinin
Center for Nanophase Materials Sciences, Oak Ridge National Laboratory, Oak Ridge, TN 37831, USA
E-mail: roccapriorkm@ornl.gov, sergei2@ornl.gov

Dr. Shin-Hum Cho
Samsung Electronics, Samsung Semiconductor R&D, Hwaseong, Gyeonggi-do 18448, Republic of Korea

Dr. Delia J. Milliron
McKetta Department of Chemical Engineering, The University of Texas at Austin, Austin TX 78712, USA

Keywords: plasmonics, nanoparticles, electron beam modification, scanning transmission electron microscopy, electron energy loss spectroscopy

Spatial confinement of matter in functional nanostructures has propelled these systems to the forefront of nanoscience, both as a playground for exotic physics and quantum phenomena and in multiple applications including plasmonics, optoelectronics, and sensing. In parallel, the emergence of monochromated electron energy loss spectroscopy (EELS) has enabled exploration of local nanoplasmonic functionalities within single nanoparticles and the collective response of nanoparticle assemblies, providing deep insight into the associated mechanisms. However, modern synthesis processes for plasmonic nanostructures are often limited in the types of accessible geometry and materials and are limited to spatial precisions on the order of tens of nm, precluding the direct exploration of critical aspects of the structure-property relationships. Here, we use the atomic-sized probe of the scanning transmission electron microscope (STEM) to perform precise sculpting and design of nanoparticle configurations. Using low-loss EELS, we provide dynamic analyses of evolution of the plasmonic response. We show that within self-assembled systems of nanoparticles, individual nanoparticles can be selectively removed, reshaped, or patterned with nanometer-level resolution, effectively modifying the plasmonic response in both space and energy. This

process significantly increases the scope for design possibilities and presents opportunities for arbitrary structure development, which are ultimately key for nanophotonic design.

1. Introduction

Spatial confinement of matter in functional nanoparticles has propelled these systems to the forefront of a variety of fields in nanoscience and nanotechnology.[1–4] Nanoparticles offer an excellent environment for exploration of fundamental physical and chemical phenomena due to their extreme degrees of tunability.[5–7] As a result, they have been applied in a variety of fields ranging from nanophotonics, quantum optics, catalysis, medicine, mechanical or optical coatings, to surface enhanced Raman spectroscopy (SERS).[8–13]

Nanoparticles on their own or in few-particle clusters exhibit properties not found in the bulk due to a large ratio of surface area to volume; however, controlled ordering of nanoparticles assemblies allows development of new functionalities, leading to concepts such as single molecule sensing,[14] artificial molecules,[15] and molecular imaging.[16] This in turn leads to the dual challenge of preparation of nanoparticle assemblies with desired geometries and exploration of their functionalities of interest. An enormous variety of methods exist for nanoparticle synthesis including chemical synthesis and physical vapor deposition.[17–22] Electron beam lithography (EBL), focused ion beam (FIB) milling, and laser-induced dewetting methods can be used for control over material positioning and growth to some degree, but resulting particle sizes are currently too large for applications requiring particles with less than about 20 nm as the critical dimension. Colloidal self-assembly of nanocrystals is a chemical growth alternative that allows for high packing density and high-quality nanoparticle ordering for particle sizes below 10 nm and has been thoroughly reviewed,[23] but in general, the particle chemistry, stoichiometry, morphology and relative position largely cannot be locally modified after the assembly process, which hinders opportunities to explore phenomena that depend on these traits.

Perhaps the best way to extend the correlations between structure and properties is through a combination of these methods via controllable modification of synthesized plasmonic material. Intentionally modifying the plasmonic structures dynamically after synthesis has largely not been explored. Direct-write techniques such as EBL and FIB have high degrees of precision, and can be used for patterning down to the ~1 nm level with an aberration corrected beam in specific geometries.[24] An even higher-precision alternative is the electron beam of the scanning transmission electron microscope (STEM). It is well known that the beam can modify the material, often in an undesirable[25] manner, however the beam-sample interaction can also be exploited to directly control and manipulate materials down to the single-atom level.[26–29] The electron beam can also be used to create larger scale nanostructures, for example by milling nanowires to tune plasmonic resonances.[30]

From a characterization perspective, the breakthrough in investigating plasmonic behavior of individual and few nanoparticle systems resulted from advances in monochromated electron energy loss spectroscopy (EELS) in an aberration corrected STEM. This route has enabled direct visualization of the spatial distribution of plasmon resonances in metallic and semiconducting nanocrystals,[31–33] helped discover that detected resonances in quantum nanoparticles were different than original theoretical predictions,[34] and more recently, allowed distinguishing between different elemental isotopes via so-called aloof spectroscopy.[35] These experiments, however, rely on pre-existing as-synthesized nanoparticle geometries and thus only a limited degree of exploration is possible.

Here we demonstrate the in-situ control of three-dimensional plasmonic structures within the framework of a self-assembled monolayer of nanoparticles using an electron beam in a STEM, where the electron beam is accelerated to 60 kV and is aberration corrected up to 5th order. In contrast to previous work on manipulating two-dimensional materials with the STEM,[36,37] here the combination of STEM and EELS allows us to explore a significant degree of in-plane structural variation, dynamically tune plasmon resonances, and examine the chemical and plasmonic evolution during in-situ three-dimensional nanoparticle manipulation.

2. Experimental Details

The material being studied is a self-assembled monolayer of chemically synthesized F,Sn:In_2O_3 semiconductor nanoparticles with a typical dimension of 10 nm. These nanoparticles offer an ideal platform for spectrally tuning plasmonic responses based on electron donation from Sn and F dopants[38] that are spectrally far from the inter-band transition. Therefore, plasmon modes can be unambiguously identified. Here, F concentration is fixed while Sn content varies between 0% and 10%, where 0% Sn forms cubic nanoparticles and 10% Sn forms spherical ones. The STEM used to sculpt the nanoparticles is also used to analyze the modifications by EELS, allowing a fast and convenient testing ground for both chemical analysis via acquiring core loss energy signals in real time, and plasmonic analysis via low-loss energies. Specifically, the modification and in-situ core-loss EELS are carried out at high current, while the (monochromated) low-loss EELS analysis is conducted at roughly 20x lower beam current.

A typical high angle annular dark field (HAADF)-STEM image of a self-assembled monolayer of nanocubes is shown in **Figure 1** (a), highlighting that, even in a close to best-case scenario, a large degree of heterogeneity and randomness is present in the system. Since the particle sizes fluctuate around a nominal average of 10 nm, size-dependent effects may play a significant role in the plasmonic response, such that slight deviations in particle size have a strong impact.[39,40] The nanoparticle array itself supports several plasmon modes, most of which are hybridized modes and difficult to analyze due to their collective nature and spatial overlap.[41] However, when a defect in the array (e.g., an edge or a missing nanoparticle) is encountered, the electric field strength and thus the plasmonic response at certain energies is greater. This is important for many applications that require an enhanced field strength in a specific location that, as we will show, can be achieved by manipulation of a nanoparticle's position using the electron beam.

Several hallmark examples of nanoparticle modifications are presented in Figure 1. First, we generate features by removing other particles surrounding the intended feature; Figure 1(b) shows a 1-D chain; Figure 1(c) shows a split-ring resonator – an element useful in nanophotonics and metamaterials. Different checkerboard patterns illustrate periodic plasmonic hotspots, Figures 1(e) and (f). Alternatively, particles may be fused together under different scanning schemes (Figure 1(g)). The use of the electron beam in these ways allows tremendous flexibility in post-fabrication and enables the ability to tune the location of nanoparticles as well as their plasmonic spatial features. While we measure changes in plasmonic properties, we also expect other useful changes to accompany the modifications, which could hold the potential for applications in catalysis or energy-harvesting fields.

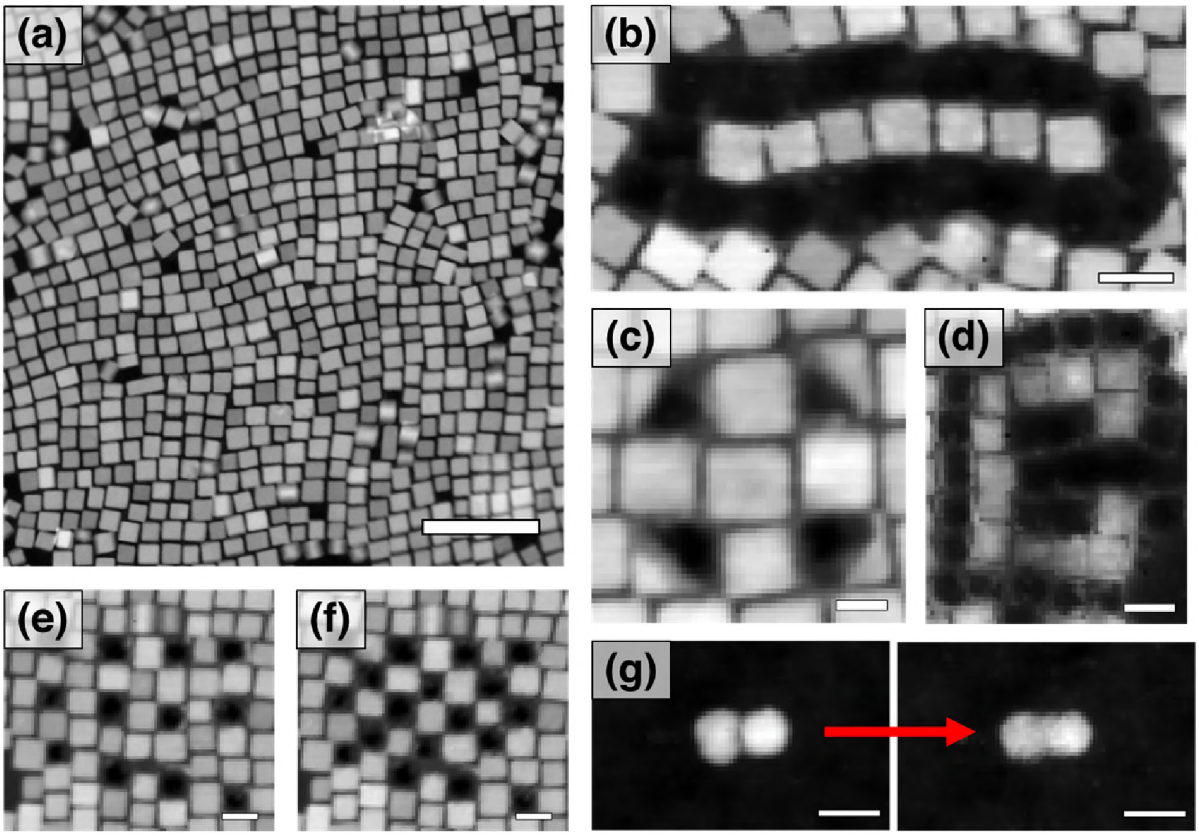

Figure 1. Examples of structural modification to nanoparticles by electron beam irradiation, visualized by HAADF-STEM images. (a) As-assembled monolayer; (b) a 1D nanochain carved out from a large array; (c) nanoparticles can be sliced diagonally or arbitrarily; (d) split ring resonator element, critical in plasmonics and metamaterial designs, constructed of nanoparticles; (e) and (f) depict various checkerboard-type schemes; (g) fusing of two isolated nanoparticles into a single nanoparticle. Scale bar in (a) is 100 nm, (c) 10 nm, all others 20 nm.

2.1. Spatial Modification

As a rough estimate, in the high-current condition, it is reasonable to assume that the electron beam diameter on the particle is on the order of Ångstroms and the beam current approaches 1 nA. These values suggest a current density of ~10^6 A/cm^2 and it is observed that the nanoparticle begins to undergo changes within minutes. This current density is roughly three orders of magnitude larger than was used with some of the first electron irradiation experiments in the STEM that were reported.[42-44] This alteration is not entirely unexpected, as electron beam damage is a common problem in (S)TEM.[45–48] However, if properly monitored and carefully performed, the electron beam irradiation can lead to desirable structural and chemical modifications. In **Figure 2**, we show the time evolution of 'spot drilling' using a focused electron beam positioned in the center of an isolated nanoparticle existing outside of an array. Figures 2 (a) and (b) demonstrate that even after completely drilling through a single particle, crystallinity is preserved in the remainder of the nanoparticle. Meanwhile, Figure 2 (c) and (d) show the plasmonic responses evolving in time after irradiation. The energy maps in Figure 2(c) and spectral features in Figure 2(d) are extracted in an exploratory fashion using non-negative matrix factorization (NMF), a technique which has been applied for the analysis of EELS data.[49] The choice of NMF is predicated on the intent to provide a consistent and accepted method for analysis of hyperspectral EELS data,[50–52] however, the extracted spectral endmembers are generally not physical – e.g., there is no guarantee their spectral shape follows a Lorentzian or Gaussian distribution. Even so, it is an excellent tool for identifying spectrally similar features in space. A similar effect is observed after irradiation when selecting and viewing EEL spectra in plasmonic hot spots (e.g., corner, edge, bulk[53]) and is shown in **Supporting Figure S2**. The nanoparticle shape changes as observed in the HAADF-STEM images acquired every 30 seconds. Two observations are critical regarding the spatial structure of the plasmon response: first, the so-called "corner mode" in NMF component 1 develops into an all-around surface feature rather than being prominent only at the corners; second, a new feature manifests as a localized region in the particle center in NMF component 2 that initiates after irradiation for ~60 seconds. The bulk mode in NMF component 3 remains relatively unchanged, which indicates we have selectively altered the spatial distribution of specific plasmon modes, leaving some modes unaffected, and introduced a new region of electric field intensity within the nanoparticle – note the EEL spectra do not directly represent the electric field but rather the photonic density of states.[51] While the hybridization model has been shown to explain the emergence of mode splitting and consequently new plasmonic features, [54,55] the observed changes here are primarily in space. The three NMF components, in general, do not exhibit a change in their spectral peak position. Of critical importance here is the fact that the relative intensities of the spectral endmembers do not decrease substantially after irradiation. While the NMF 1 spectral component decreases slightly, it can be argued this is due to the mode being spread out over the particle surface rather than concentrated in the corners. However, the bulk resonance (NMF 3) does decrease by about half, while the surface plasmon edge mode (NMF 2) essentially remains the same, suggesting the possibility of tailoring specific plasmon modes within a single structure.

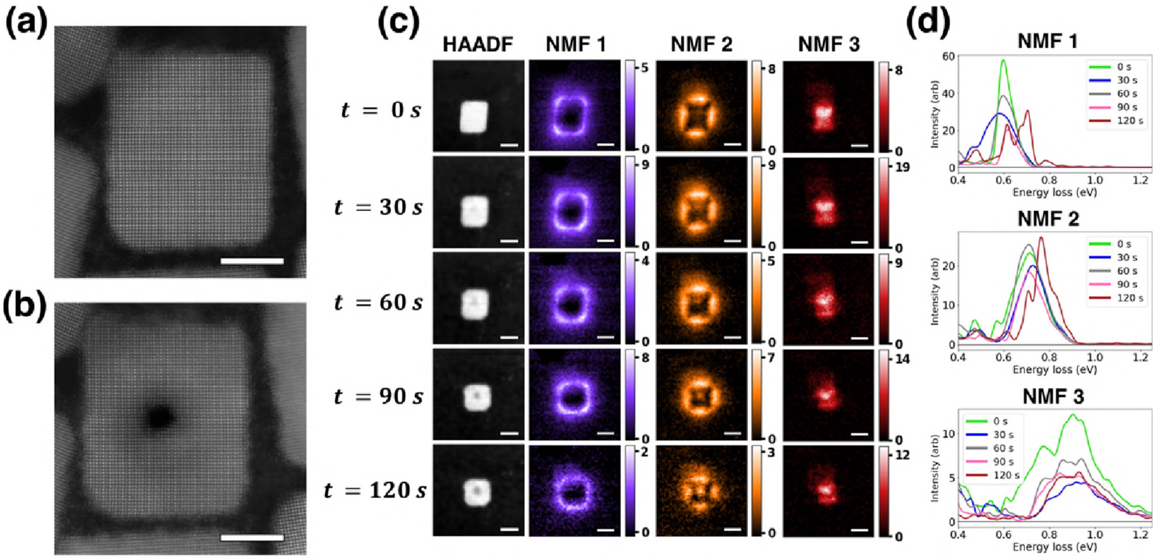

Figure 2. Spot drilling on an isolated nanoparticle. HAADF-STEM images acquired at low current showing crystal structure before drilling (a), and after drilling (b); large portion of nanoparticle retains crystallinity. HAADF-STEM images in (c) shown as a function of drilling center of nanoparticle, with NMF deconvolution performed in spectral domain to assess changes in plasmonic response due to spot drilling. Dominant three NMF abundance maps shown for each time step in (c), while corresponding NMF spectral endmembers, which are Gaussian blurred for clarity, shown in (d). Note that propensity of NMF method is used to separate different symmetries in spatial plasmonic maps; NMF endmembers illustrate evolution of corresponding behaviors during modification. Scale bar in (a) and (b) is 5 nm, all scale bars in (c) are 10 nm.

The fact that the crystallinity of the drilled particle (and consequently any nearby particle) remains intact is crucial for retaining intense plasmon features. A larger field of view showing the preservation of crystallinity in nearby particles is shown in **Supporting Figure**

S3. However, we also observe that once a hole has been drilled, the particle seems to be in a weakened state near the surface of hole, as even a lower current electron probe can enlarge the hole size with relative ease. We postulate that the atoms at the hole interface are left in a destabilized bonding state and therefore can be easily swept away by even a low intensity probe, though perhaps an in-situ or ex-situ annealing step can assist in forming a more strongly bonded inner hole surface after irradiation. **Figure 3** shows a drilling progression in time demonstrating that selective removal can approach single atomic column resolution. Close inspection in Figure 3 (a-b) of drilling through a 10-15 nm thick nanoparticle first reveals that it may be possible to selectively remove even a single column of atoms, however nearby columns are also partially removed due to the nature of a converged probe. Second, during early drilling steps, the particle appears to heal – similar to what has been reported in graphene.[56] We suspect this may be due to high-resolution image acquisition between each drilling step and may cause surface atoms to be ionized or dislodged and tracked into the hole. To visualize the electron beam's milling spatial profile, we plot a few of the surfaces in Figure 3 (c), obtained by applying a moderate Gaussian filter to the HAADF-STEM images and using these intensities to construct a 3D surface – the original image is then mapped to this surface. From this we can see that while there is certainly a conical shape, the slope appears to increase the larger the hole becomes, indicating the practical resolution that can be achieved and ultimately that sculpting three-dimensional objects is indeed possible with atomic-scale precision.

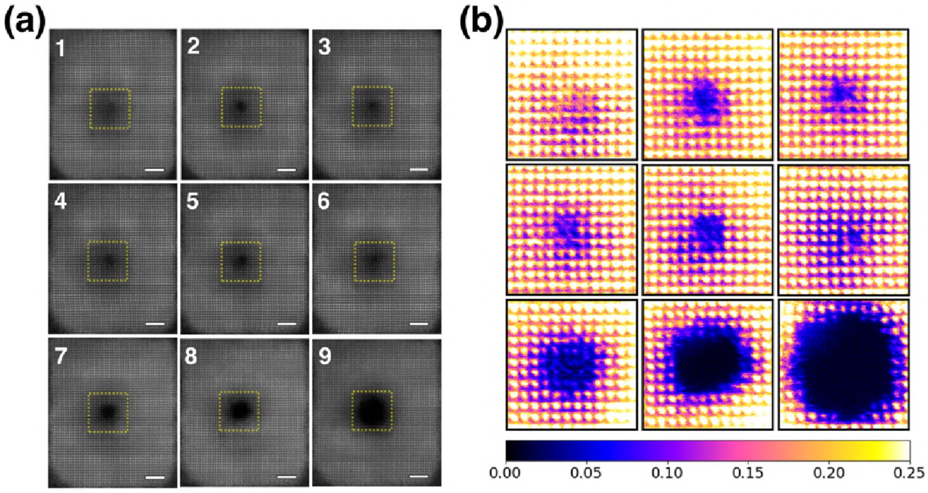

Figure 3. Electron beam milling of 3D structure. Due to use of a converged beam and thickness of structure, a conical profile is expected, thus limiting the final resolution. (a) shows HAADF-STEM image time series (1-9) of spot-drilling single nanoparticle, in 30 second increments at slightly reduced current; (b) enlarged view of regions from (a) with contrast adjusted to view loss of atoms; (c) surface plot of selected time steps. Scale bars 2 nm.

Nanoparticle removal can be performed using either a highly focused beam which scans a defined region, or a defocused beam fixed on the equivalent region – we note that the present authors have had more success with scanning a focused beam. It is also critical to note that a nanoparticle need not be completely drilled through or removed – instead, by reducing beam dwell time, one may choose to partially remove the material, in fact this can be seen in the HAADF-STEM images in Figures 2, 3, and Figure S1. However, this process still effectively modifies the shape, which in turn has an effect of the plasmon resonance. Another relevant aspect to consider is the reproducibility of the modifications. In general, the target design is usually reached, but it should be clear that not all particles respond identically to interaction with the electron beam (e.g., due to different crystal orientations, slightly different chemical variability, etc.). Sample drift is also a concern for processes that occur over several minutes. In other words, feedback is ultimately required for best reproducibility – this can be carried out by periodic HAADF-STEM imaging to manage drift, ensuring the beam is in the correct position, and monitor the progress.

2.2. Spectral modification

Engineering the plasmon distribution in dimensions of both space and energy is also possible. We illustrate this effect by illuminating a particle dimer pair with a defocused probe whose beam diameter slightly exceeds that of a single nanoparticle. The probe is then placed between the two particles with the intention of fusing the particles into a single unit. This process is shown in discrete time intervals in **Figure 4**, where it is clear in the structural HAADF-STEM image that the particle shape is changing.

It is not surprising that the particle could become contaminated or rearrange its atomic configurations (e.g., reduced crystallinity) upon beam irradiation. Contamination alters the dielectric environment of the nanoparticle and in doing so, effectively reduces the intensity of the plasmon responses. Since particles originally sustain atomically smooth surfaces and are single crystal, polycrystallinity or increased roughness will also cause the response to become weaker by electron scattering losses at increased number of boundaries. To study the exposure effect in a manner that allows spatial exploration of plasmonic activity, we perform NMF deconvolution on each dataset, and show the first and second NMF components at each time step. The NMF components show that the plasmon modes red-shift as a function of melding. Over the entire 3-min. exposure, we measure a 0.22 eV and a 0.14 eV redshift for components 1 and 2, respectively. In the **Supporting Figure S4**, raw spectra from selected regions of interest are shown to strengthen the argument for a true redshift of the plasmon resonances. This is similar to the effect of reducing the distance d between particles, where the distance dependence and potential degree of overlap have been shown to have a direct impact on the plasmon resonance energy.[57] We again draw attention to the behavior that after electron irradiation, the surface resonances are more strongly affected than the bulk resonance. As will be discussed later, the reason for this difference may be chemical in nature.

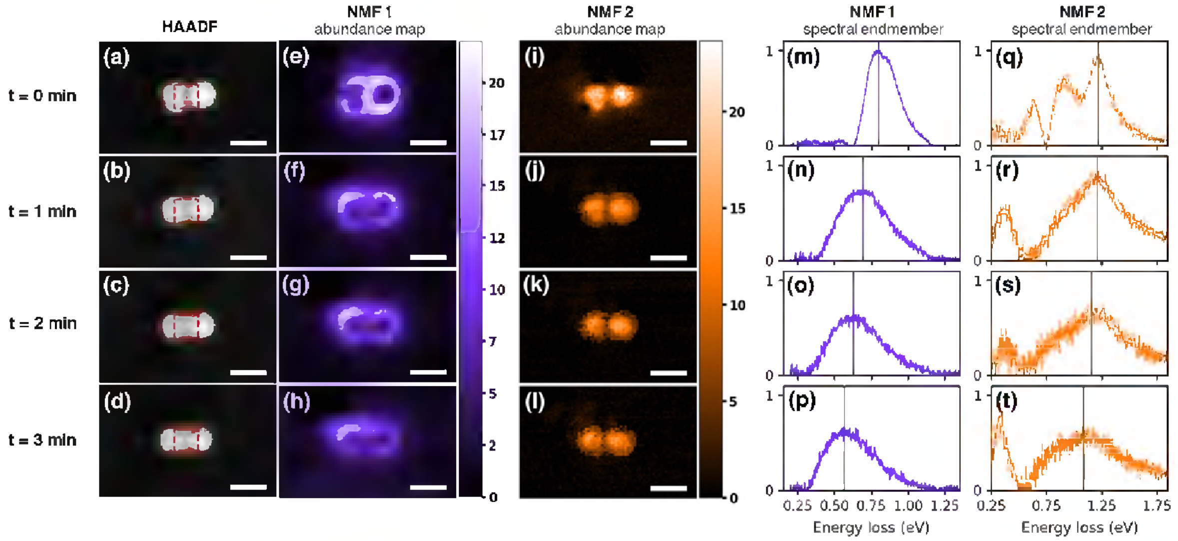

Figure 4. Effect of electron beam exposure on structure and plasmon resonance of a dimer configuration. HAADF-STEM images are shown in (a-d); 1st NMF and 2nd NMF abundance maps for each time increment are shown in (e-h) and (i-l), respectively; 1st NMF and 2nd NMF spectral endmembers for each time increment are shown in (m-p) and (q-t), respectively, normalized to strongest mode. Beam was defocused and placed in region between nanoparticles to promote fusing, shown by the dashed region in the HAADF-STEM images. Black vertical lines in (m-t) indicate spectral peak position of dominant feature for plasmon mode of interest. All scale bars are 20 nm.

2.3 Complex structures

We also utilize the self-assembled array as a basis to create more complex structures since the array supports a wide range of plasmon modes that represent collective responses of the entire system. In the vicinity of a defect such as an edge or missing particle within the array, the plasmonic response extends into this space with high intensity. This effect is crucial for many applications that require an enhanced field strength in a specific location that, as we will show, can be achieved by manipulation of a nanoparticle's position using the electron beam. To illustrate the spatial modification to the plasmonic features, in **Figure 5** we selectively remove particles to produce specifically designed structures, e.g., the ORNL logo in Figure 5 (a), or a checkerboard type pattern in Figure 5 (b). The plasmonic effects of other geometries shown in Figure 1 are presented in **Supporting Figure S5**. The result is strong plasmonic intensity at selectable locations with nanoscale resolution, which is induced by selectively removing nanoparticles from the array. The NMF components highlight the different regions of plasmonic activity; and their associated spectral features are also shown in color.

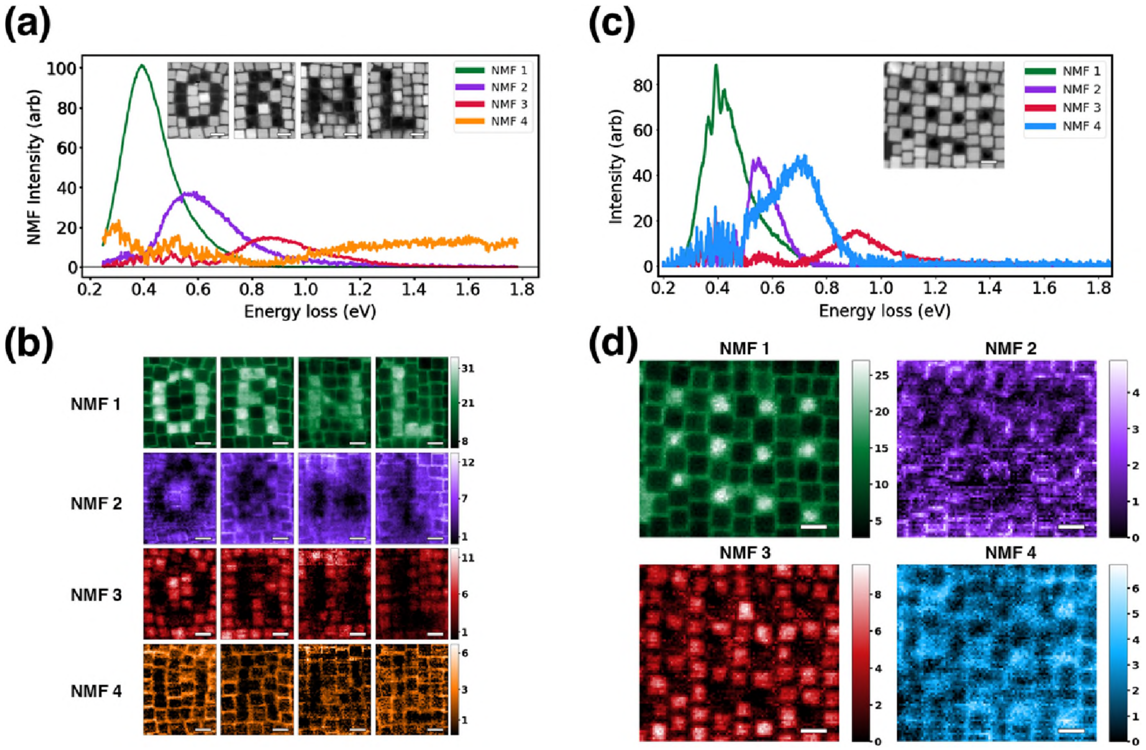

Figure 5. Examples of spatial modification of plasmon responses. (a) and (b) show laboratory logo “ORNL” shaped by electron beam; four dominant NMF spectral features with corresponding spatial maps are shown in (a) and (b) respectively; (c) and (d) depict periodic control in the form of a checkerboard pattern and dominant NMF components emphasize resulting spatial localization of different plasmon modes. HAADF-STEM images of each pattern are insets in (a) and (c). Color schemes are the same for similar spectral features, but not all features are identical. NMF separates feature in (c) and (d) near 0.6 eV into two distinct components (purple, blue), where in (a) and (b) it keeps it as one, allowing a fourth and different feature to be extracted (orange). Scale bars are all 20 nm.

Perhaps not immediately obvious but nonetheless notable is the fact that the resonances are controlled in several different ways, for example, by removing a particle, a void is created where the plasmonic intensity (of the lowest energy mode) is still strongly observed. At the same time, there is nothing to support any localized surface or bulk modes at that location. This change in response is illustrated by the various components’ spatial maps in Figure 5. In Figure 5 (a), NMF 1 (green) shows the collective plasmon mode that normally is evenly distributed across a regular array. However, due to the creation of defects (i.e., removal of particles in the array), we find that the delocalized surface plasmon array mode extends into these defects, allowing us to create localized plasmonic voids where the array mode is still strongly activated, but the localized surface and bulk modes are no longer present. In other words, this enables us to modify the overall structure of the plasmon response. Note that comparison of the four NMF features extracted in Figure 5 shows a discrepancy between the two examples – specifically, NMF 2 in Figure 5 (a,b) appears to be a combination of NMF 2 and 4 in Figure 5 (c,d). Because of this, Figure 5 (a,b) have an additional spectral component (NMF 4) which is not observed in Figure 5 (c,d) – this is only because we chose to be consistent in the number of components used in the model (four) and this should not be misinterpreted as any sort of different physical effect.

A careful examination of the distance dependence of the plasmonic intensity is illustrated in **Supporting Figure S6**. Presenting the response as shown in Figure 5 merely serves to emphasize the spatial control of specific energy modes. Similar effects are shown for the checkerboard pattern in Figure 5(b), where emphasis is placed on the ability to generate periodic spatial structures. The resulting localized plasmon resonances in these periodic checkerboards are spectrally similar, but their locations in space are controlled.

Removal of particles in this manner is similar to the engineering of so-called “gap surface plasmons” (GSPs) where an optically thick (~150 nm) conductive film has a slot milled into it which, if appropriately designed, supports a propagating plasmon mode.[58,59] There, the geometry of the slot plays a role in the possible GSP modes that may exist. The array mode that exists due to the collective interaction of many particles closely resembles the propagating surface plasmon mode at a metal-vacuum interface. In this way, a monolayer of self-assembled nanoparticles can be regarded optically as a thin film. In **Supporting Figure S7**, we show an analysis of different “slot” lengths, where the resonance energies in principle should depend on the length of the slot. We do not observe any geometric dependent EELS features from this analysis, however, in **Supporting Figure S8** we compare the EELS differences between the created voids and pre-existing gaps in the array and do find there to be an increased intensity in the created voids (~15%), even after consideration of elastic scattering differences from potential silicon nitride removal where voids are located, which does hint at the gap mode possibility. It is entirely possible this is a situation where both a gap mode and array mode exist, however evidence of the GSP is inconclusive mainly because the entire specimen is electron transparent.

Irradiation of a material by the electron beam can involve several processes[60] dependent on the electron beam energy, the probe current, the material system, the support, etc. In an effort to determine the primary mechanism responsible for the deliberate changes, we employed several different accelerating voltages. The substrate, a 15-nm thick silicon nitride membrane, remains the same in all cases. We did not observe a strong dependence on beam energy (60-200 kV) with the beam current kept constant at ~0.5 nA for particle removal; however, these experiments show a clear dependence on current, i.e., increasing probe current hastens particle removal. Little to no dependence of modification on beam energy coupled with the fact that we are using metal-oxide host nanoparticles leads us to deduce the most likely mechanism is a combination of knock-on damage and radiolysis.[61] The oxygen can be ionized or knocked out of the host particle, both of which destabilize the nanoparticle bonds and allow non-oxygen species to be subsequently removed. A detailed understanding of the mechanism behind the nanoparticle removal by the electron beam is not the intent of this work, however, we are able to trace the chemical evolution, which offers insight into the origins of the plasmonic feature modifications.

We explore the chemical and physical changes occurring in individual nanoparticles as well as nearby nanoparticles. For nanoparticles that are completely or partially removed, a primary concern is redeposition of the removed material and general contamination of nearby nanoparticles. From an EELS analysis of both low loss and core loss energy signals, we show in **Supporting Figure S9** that the chemical composition of nearby particles is preserved. We speculate that the material may be entirely removed from the system since we also observe the removal of the underlying silicon nitride membrane. The substrate removal was a little surprising, as Ref [62] suggests a minimum beam energy of 150 kV is required to drill through amorphous silicon nitride, but this is likely due to the effect of our high current density for drilling and ultra-high-vacuum conditions. Otherwise, if partially drilling a particle, the removed material will be in an amorphous state and can migrate around the surface of the local sample region based on the probe location. We also note the presence of a small amount of carbon contamination that appears to coat all nanoparticles uniformly, but this is present even in regular imaging conditions far from any regions that were sculpted.

To address the question of which elemental species are removed and where they might go, we perform time-resolved EELS, which are shown as part of the supporting information. For nanoparticles that are partially drilled, or for those that are fused together, this time dependent analysis is performed by capturing the local core loss EELS signal during the irradiation process. In **Supporting Figure S10**, the time dependence of the core loss EELS in 20 s intervals is shown, where the EEL spectrum has been acquired every 1 s and integrated over 20 s. From Figure S10 (a), the indium $M_{4,5}$ edge is observed to decrease significantly after close to two minutes of exposure, while the oxygen K edge is steadily reduced throughout the entire experiment. Calculation of the ratio of EEL edge intensities of oxygen to indium in Figure S10 reveals that initially, the oxygen is removed, and only until near two minutes of exposure does the indium drastically and preferentially begin to be removed, suggesting at least a two-part mechanism where the second stage of indium removal occurs only after a destabilizing removal of oxygen. Notably, both indium and tin have very low melting points. It is certainly possible we are removing the F alternatively, as this is a dopant and tends to be easily removed by electron beam, and may also explain the red-shifting behavior due to lack of electron donation. Unfortunately, the core loss EEL signature of Fluorine is difficult to detect. In any case, the preferential removal of different elements might present opportunities for the direct chemical engineering of atomic structures; as well as an enhanced scope for plasmon engineering via local control of the conduction electron levels. Note that the capability also exists to preferentially alter the particle's surface chemistry compared to its volume, e.g., either by rastering across a large area of the particle or by fixing the probe to a small region.

Considering the observation that the indium (or fluorine) content is preferentially modified suggests that the conduction electrons supporting the plasmon resonances will be decreased due to reduced metallic character in the nanocrystals. Since we have already shown that a majority of the crystallinity is preserved, redeposition of removed material into an amorphous state covering the particles can explain the partially reduced plasmon intensity and is in general not overly surprising. We also expect the beam to attract carbon contamination onto the surface of the nanocubes, further dampening the plasmon response. What is peculiar and of great potential utility is the spectral shifting of the plasmon signals after irradiation. Spectral tunability in metal nanoparticles is generally accomplished via particle size and shape tuning, however it is also possible to tune plasmon resonances by adjusting the number of conduction electrons in the material, for example by doping.[38] Here, we instead altered the concentration of conduction electrons in the material by using the electron beam, and also have the ability to modify the shape; thus, this work presents two nanoscale methods for tuning the resonant frequencies.

The degree to which the resonance energies can be shifted is relatively significant given the original energies, however, one may naturally question to what extent can this be shifted and what approaches can be used to exploit it further. This work focused solely on the metal-oxide plasmonic particles, specifically indium-oxide, so a next logical experiment would make use of other conductive metal oxides – for example, zinc oxide or silver oxide nanoparticle composites.[63,64] These materials in particular have higher energy resonances, and if we assume that a similar, proportional energy shift occurs upon electron irradiation, then this could open the door toward a much wider range of tunability. Incorporation of increased dopant material may also provide an increased range of tunability.

This modification scheme presents several different opportunities. First, this process could likely be scaled up to the industrial level in a conventional electron-beam writing system readily used in multi-centimeter scale photomask manufacturing processes, given that the modification has been demonstrated to occur at 60 kV and most dedicated e-beam writing systems operate in the 50-100 kV range. We also note that in electron beam *lithography,* a primary resolution barrier is due to scattering within the electron beam resist or the proximity effect – both of which are not a concern here since this is not a lithographic approach.[66] In this way one could design a large-scale structure that is directly (i.e., without resist) modified on the nanoscale, or possibly even the atomic scale, by an electron beam writing system. Secondly, this route could also be beneficial to modification of devices such as qubits or quantum emitters where a single or small number of devices make a difference. Finally, the modified structures are stable in atmospheric conditions which allows for more flexibility in a variety of applications.

3. Conclusion

Future studies will examine these effects for electron beam irradiation in other metal oxide plasmonic and noble metal nanoparticles. We postulate that it is the more complex chemical structure of the oxides here that allows such a chemical modification of the plasmonic structure and attempts to repeat similar experiments in noble metal nanoparticles might produce different results. We would likely not expect to modify the spectral position of the resonances in single-element nanoparticles in the same way. As such, the average concentration of conduction electrons would not change upon removal of small amounts of noble metal atoms, and for this reason, we suspect this chemical effect has not been previously reported.

In summary, we have shown that sculpting of the plasmonic properties of nanoparticles with a resolution better than 1 nm is possible using a high-energy focused electron beam under appropriate conditions. A great degree of flexibility is enabled, allowing particles to be either partially removed, completely removed, fused together, and, if desired, selectively modified in terms of chemistry and crystal structure. Precise removal of nanoparticles enables the design of increasingly complex nanophotonic and plasmonic systems by dynamically modifying as-assembled structures on-the-fly. Critically, the plasmonic responses of the nanoparticles were modified in the spatial domain, producing unique plasmonic systems, which carry a corresponding change in their energy response. Irradiation by an electron beam was demonstrated to have different effects depending on critical factors, such as electron dose imparted to a nanoparticle, area of irradiation, amount of defocus, etc. Importantly, chemical and plasmonic analysis can be carried out seamlessly by EELS at different energy scales immediately following the electron beam modification.

Moving on from tailoring the spatial response, we envision an automated experiment where a particular plasmonic feature can be specifically designed and subsequently engineered by precise automated control and feedback of the electron beam. Recent work using encoder-decoder neural networks[67] demonstrated extraction of the correlative relationship between the local particle geometry and plasmonic response. Hence, we aim to generate custom responses where the network predicts the required geometry and then, as shown here, we deliberately sculpt such a geometry using e-beam particle modification methods to match that template. The future automation of this experiment will allow a deeper exploration into fully customizable and almost arbitrary plasmonic behavior, and process automation will lead to a significantly faster, accurate, and, perhaps most important of all, reproducible results.

4. Methods

Materials:

Indium (III) acetate (In(ac)$_3$, 99.99%), Tin (IV) acetate (Sn(ac)$_4$), Oleic acid (OA, 90%, technical grade), Oleyl alcohol (OlAl, 85%, technical grade) were purchased from Sigma-Aldrich. Tin (IV) fluoride (SnF$_4$, 99%) was purchased from Alfa Aesar, Hexane (99.9%), Isopropyl alcohol (99.5%, Certified ACS), were purchased from Fisher Chemical. All chemicals were used as received without any further purification.

Fluorine Doped Indium Tin Oxide (FT:IO, F,Sn:In$_2$O$_3$) Nanoparticle Synthesis:

All synthesis procedures are undertaken by employing standard Schlenk line techniques using a modification of previously reported methods for continuous slow injection synthesis of indium oxide nanoparticles.[20] 29,46 In(ac)$_3$ 1342.97 mg (4.6 mmol), SnF$_4$ 48.68 mg (5%, 0.25 mmol), Sn(ac)$_4$ 53.23 mg (3%, 0.15 mol), and oleic acid (10 ml) are loaded in a three-neck round-bottom flask in a N2-filled glove box. The precursors are stirred with a magnetic bar at 600 rpm and degassed under vacuum at 120 °C for 15 min. The injection solution is added at rate of 0.2 ml/min, into 13 ml of oleyl alcohol maintained at 290 °C vented with a 19-gauge needle under inert N2 gas flow. The reaction mixture turns blue a few minutes into the injection. Subsequently, growth is terminated by removal of the heating mantle and cooled by blowing air on the three-neck flask vessel. The nanoparticles are dispersed in hexane, then isopropyl alcohol antisolvent is added and the mixture is centrifuged at 7500 rpm for 10 min. The washing procedure is repeated 3 times and the nanoparticles are redispersed in 10 ml of hexane. The resultant nanoparticle dispersion is centrifuged at 2000 rpm for 3 min to remove non-dispersible aggregates and the supernatant is collected as the nanoparticle stock sample. For spherical particle sample, concentration series of 10 % Sn(ac)$_4$ doped F,Sn:In$_2$O$_3$

nanoparticle was synthesized by controlling the $Sn(ac)_4$ to $In(ac)_3$ molar precursor ratio, while SnF_4 was maintained at 5% molar ratio, keeping other reaction parameters identical. Monolayer nanocrystal arrays were deposited onto a SiN TEM grid via Teflon trough liquid-air interface self-assembly. Native surface ligands were removed from the nanocrystal assembled array by TEM grid Ar plasma cleaning for 15 min.

Imaging, spectroscopy, and modification:

For low-loss EEL spectroscopy and HAADF-STEM imaging, a monochromated aberration-corrected NION microscope was operated at an accelerating voltage of 60 kV, with a probe current on the order of 20 pA, and a convergence angle of 30 mrad. The full width half maximum of the zero loss peak (ZLP) after monochromation was ~50 meV, with the potential to be reduced to as low as 5 meV, however this was kept higher to maintain a high signal to noise ratio. Post processing of the acquired low-loss EEL spectra to remove the zero-loss peak and the phonon signal arising from the silicon nitride support membrane was performed by fitting a two-term exponential power law to the zero-loss peak, and truncating the energy axis below 200 meV, respectively. For core-loss EEL spectroscopy and modification processes, the electron beam was no longer monochromated, allowing a probe current on the order of 500 pA. In all cases, the sample pressure is kept at a stable 10^{-9} Torr.

Supporting Information

Supporting Information is available from the Wiley Online Library or from the author.

Acknowledgements

This effort is based upon work supported by the U.S. Department of Energy (DOE), Office of Science, Basic Energy Sciences (BES), Materials Sciences and Engineering Division (K.M.R., S.V.K.) S.H.C and D.J.M. acknowledge (NSF CHE-1905263, and CDCM, an NSF MRSEC DMR-1720595), the Welch Foundation (F-1848), and the Fulbright Program (IIE-15151071). Electron microscopy was performed using instrumentation within ORNL's Materials Characterization Core provided by UT-Battelle, LLC, under Contract No. DE-AC05- 00OR22725 with the DOE and sponsored by the Laboratory Directed Research and Development Program of Oak Ridge National Laboratory, managed by UT-Battelle, LLC, for the U.S. Department of Energy.

Author Contributions

K.M.R. conducted the microscopy, performed analysis, and wrote the manuscript. S.H.C synthesized the samples and help write the manuscript. A.R.L enabled the optimal beam control, helped consider additional experimental methods and helped write the manuscript. D.J.M. helped write the manuscript. S.V.K. conceived and oversaw the project, and helped write the manuscript. We thank Jordan Hachtel for his insightful discussions and invaluable advice.

Conflict of Interest

The authors declare no conflict of interest.

Received: ((will be filled in by the editorial staff))
Revised: ((will be filled in by the editorial staff))
Published online: ((will be filled in by the editorial staff))

References

[1] A. P. Alivisatos, *Science* **1996**, *271*, 933–937.

[2] M. V. Kovalenko, L. Manna, A. Cabot, Z. Hens, D. V. Talapin, C.R. Kagan, V. I. Klimov, A. L. Rogach, P. Reiss, D. J. Milliron, P. Guyot-Sionnnest, G. Konstantatos, W. J. Parak, T. Hyeon, B. A. Korgel, C. B. Murray, W. Heiss, *ACS Nano* **2015**, 1012–1057.

933–937 (1996).

2. Kovalenko, M. V. *et al.* Prospects of Nanoscience with Nanocrystals. *ACS Nano* **9**, 1012–1057 (2015).

[3] D. V. Talapin, J.-S. Lee, M. V. Kovalenko, E. V. Shevchenko, *Chem. Rev.* **2010**, *110*, 389–458.

[4] X. Michalet, F. F. Pinaud, L. A. Bentolila, *Science* **2005**, *307*, 538–544.

[5] J. A. Fan, C. Wu, K. Bao, J. Bao, R. Bardhan, N. J. Halas, V. N. Manoharan, P. Nordlander, G. Shvets, F. Capasso, *Science* **2010**, *328*, 1135–1138.

[6] P. Yang, J. Zheng, Y. Xu, Q. Zhang, L. Jiang, *Adv. Mat.* **2016**, *28*, 10508–10517.

[7] A. Agrawal, S.-H. Cho, O. Zandi, S. Ghosh, R. W. Johns, D. J. Milliron, *Chem. Rev.* **2018**, *118*, 3121–3207.

[8] M. S. Tame, K. R. McEnery, S. K. Özdemir, J. Lee, S. A. Maier, M. S. Kim, *Nature Physics* **2013**, *9*, 329–340.

[9] A. Corma, H. Garcia, *Chem. Soc. Rev.* **2008**, *37*, 2096–2126.

[10] D. Lee, M. F. Rubner, R. E. Cohen, *Nano Lett.* **2006**, *6*, 2305–2312.

[11] D. Bobo, K. J. Robinson, J. Islam, K. J. Thurecht, S. R. Corrie, *Pharm Res* **2016**, *33*, 2373–2387.

[12] P. K. Jain, X. Huang, I. H. El-Sayed, M. A. El-Sayed, *Plasmonics* **2007**, *2*, 107–118.

[13] A. Otto, H. Grabhorn, W. Akemann, *J. Phys.: Condes. Matter* **1992**, *4*, 1143–1212.

[14] S. S. Aćimović, M. P. Kreuzer, M. U. González, R. Quidant, *ACS Nano* **2009,** *3*, 1231–1237.

[15] H. Wang, D. W. Brandl, P. Nordlander, N. J. Halas, *Acc. Chem. Res.* **2007**, *40*, 53–62.

[16] J.-H. Lee, Y.-M. Huh, Y. Jun, J. Seo, J. Jang, H.-T. Song, S. Kim, E.-J. Cho, H.-G. Yoon, J.-S. Suh, J. Cheon, *Nat. Med.* **2007**, *13*, 95–99.

[17] D. J. Milliron, S. M. Hughes, Y. Cui, L. Manna, J. Li, L.-W. Wang, A. P. Alivisatos, *Nature* **2004**, *430*, 190–195.

[18] M. Grzelczak, J. Pérez-Juste, P. Mulvaney, L. M. Liz-Marzán, *Chem. Soc. Rev.* **2008**, *37*, 1783–1791.

[19] P. A. Pandey, G. R. Bell, J. P. Rourke, A. M. Sanchez, M. D. Elkin, B. J. Hickey, N. R. Wilson, *Small* **2011,** *7*, 3202–3210.

[20] E. V. Shevchenko, D. V. Talapin, N. A. Kotov, S. O'Brien, C. B. Murray, *Nature* **2006**, *439*, 55–59.

[21] J. D. Fowlkes, L. Kondic, J. Diez, Y. Wu, P. D. Rack, *Nano Lett.* **2011**, *11*, 2478–2485.

[22] S. J. Randolph, J. D. Fowlkes, P. D. Rack, *Crit. Rev. Solid State* **2006**, *31*, 55–89.

[23] M. A. Boles, M. Engel, D. V. Talapin, *Chem. Rev.* **2016**, *116*, 11220–11289.

[24] V. R. Manfrinato, A. Stein, L. Zhang, C.-Y. Nam, K. G. Yager, E. A. Stach, C. T. Black, *Nano Lett.* **2017**, *17*, 4562–4567.

[25] R. F. Egerton, *Ultramicroscopy* **2013**, *127*, 100–108.

[26] O. Dyck, S. Kim, S. V. Kalinin, S. Jesse, *Appl. Phys. Lett.* **2017**, *111*, 113104.

[27] O. Dyck, S, Kim, E. Jimenez-Izal, A. N. Alexandrova, S. V. Kalinin, S. Jesse, *Small* **2018**, *14*, 1801771.

[28] T. Susi, J. Kotakoski, D. Kepaptsoglou, C. Mangler, T. C. Lovejoy, O. L. Krivanek, R. Zan, U. Bangert, P. Ayala, J. C. Meyer, Q. Ramasse, *Phys. Rev. Lett.* **2014**, *113*, 115501.

[29] B. M. Hudak, J. Song, H. Sims, M. C. Troparevsky, T. S. Humble, S. T. Pantelides, P. C. Snijders, A. R. Lupini, *ACS Nano* **2018**, *12*, 5873–5879.

[30] L. H. G. Tizei, V. Mkhitaryan, H. Lourenço-Martins, L. Scarabelli, K. Watanabe, T. Taniguchi, M. Tencé, J.-D. Blazit, X. Li, A. Gloter, A. Zobelli, F.-P. Schmidt, L. M. Liz-Marzán, F. J. García de Abajo, O. Stéphan, M. Kociak, *Nano Lett.* **2020**, *20*, 2973–2979.

[31] S.-H. Cho, S. Ghosh, Z. J. Berkson, J. A. Hachtel, J. Shi, X. Zhao, L. C. Reimnitz, C. J. Dahlman, Y. Ho, A. Yang, Y. Liu, J.-C. Idrobo, B. F. Chmelka, D. J. Milliron, *Chem. Mater.* ***2019***, *31*, 2661–2676.

[32] V. Kapetanovic, I. C. Lazar, S. Lazar, M. J. Lagos, G. A. Botton, *Adv Optical Mater.* **2020**, *8*, 2001024.

[33] H. Yang, E. L. Garfunkel, P. E. Batson, *Phys. Rev. B* **2020**, *102*, 205427

[34] J. A. Scholl, A. L. Koh, J. A. Dionne, *Nature* **2012**, *483*, 421–427.

[35] J. A. Hachtel, J. Huang, I. Popovs, S. Jansone-Popova, J. K. Keum, J. Jakowski, T. C. Lovejoy, N. Dellby, O. L. Krivanek, J. C. Idrobo, *Science* **2019**, *363*, 525–528.

[36] B. Song, G. F. Schneider, Q. Xu, G. Pandraud, C. Dekker, H. Zandbergen, *Nano Lett.* **2011** *11*, 2247–2250.

[37] J. Lin, O. Cretu, W. Zhou, K. Suenaga, D. Prasai, K. I. Bolotin, N. T. Cuong, M. Otani, S. Okada, A. R. Lupini, J.-C. Idrobo, D. Caudel, A. Burger, N. J. Ghimire, J. Yan, D. G. Mandrus, S. J. Pennycook, S. T. Pantelides, *Nat. Nanotechnol.* **2014**, *9*, 436-442.

[38] S. H. Cho, K. M. Roccapriore, C. K. Dass, S. Ghosh, J. Choi, J. Noh, L. C. Reimnitz, S. Heo, K. Kim, K. Xie, B. A. Korgel, X. Li, J. R. Hendrickson, J. A. Hachtel, D. J. Milliron, *J. Chem. Phys.* **2020**, *152*, 014709.

[39] C. M. Staller, S. L. Gibbs, C. A. Saez Cabezas, D. J. Milliron, *Nano Lett.* **2019**, *19*, 8149–8154.

[40] S. L. Gibbs, C. M. Staller, A. Agrawal, R. W. Johns, C. A. S. Cabezas, D. J. Milliron, *J. Phys. Chem. C* **2020**, *124*, 24351–24360.

[41] S. V. Kalinin, K. M. Roccapriore, S.-H. Cho, D. J. Milliron, R. Vasudevan, M. Ziatdinov, J. A. Hachtel, *Adv. Optical Mater.* **2021**, 2001808.

[42] P. A. Crozier, M. R. McCartney, D. J. Smith, *EMAG-MICRO* **1989**, *98*, 227.

[43] T. J. Bullough, R. W. Devenish, C. J. Humphreys, *EMAG-MICRO* **1989**, *98*, 267.

[44] M. Tence, M. G. Walls, C. Jeanguillaume, C. Colliex, *EMAG-MICRO* **1989**, *98*, 311.

[45] A. L. Koh, K. Bao, I. Khan, W. E. Smith, G. Kothleitner, P. Nordlander, S. A. Maier, D. W. McComb, *ACS Nano* **2009,** *3*, 3015–3022.

[46] S. Hwang, C. W. Han, S. V. Venkatakrishnan, C. A. Bouman, V. Ortalan, *Meas. Sci. Technol.* **2017**, *28*, 045402.

[47] I. G. Gonzalez-Martinez, A. Bachmatiuk, V. Bezugly, J. Kunstmann, T. Gemming, Z. Liu, G. Cuniberti, M. H. Rümmeli, *Nanoscale* **2016,** *8*, 11340–11362.

[48] N. Jiang, *Rep. Prog. Phys.* **2015**, *79*, 016501.

[49] M. Shiga, K. Tatsumi, S. Muto, K. Tsuda, Y. Yamamoto, T. Mori, T. Tanji, *Ultramicroscopy* **2016**, *170*, 43–59.

[50] S. Zhang, C. Scheu, *Microscopy* **2018**, *67*, i133-i141

[51] A. Agrawal, A. Singh, S. Yazdi, A. Singh, G. K. Ong, K. Bustillo, R. W. Johns, E. Ringe, D. J. Milliron, *Nano Lett* **2017**, *17*, 2611-2620

[52] S. J. Barrow, S. M. Collins, D. Rossouw, A. M. Funston, G. A. Botton, P. A. Midgley, P. Mulvaney, *ACS Nano* **2016**, *10*, 8552-8563.

[53] E. P. Bellido, A. Manjavacas, Y. Zhang, Y. Cao, P. Nordlander, G. A. Botton, *ACS Photonics* **2016**, *3*, 428-433.

[54] F. J. Abajo, M. Kociak, *Phys. Rev. Lett.* **2008,** *100*, 106804.

[55] E. Prodan, C. Radloff, N. J. Halas, P. Nordlander, *Science* **2003**, *302*, 419-422

[56] E. Prodan, P. Nordlander, *J. Chem. Phys.* **2004**, *120*, 5444

[57] R. Zan, Q. M. Ramasse, U. Bangert, K. S. Novoselov, *Nano Lett.* **2012**, *12*, 3936–3940.

[58] I. Romero, J. Aizpurua, G. W. Bryant, F. J. García de Abajo, Opt. Express **2006**, *14*, 9988-9999.

[59] S. Raza, M. Esfandyarpour, A. L. Koh, N. A. Mortensen, M. L. Brongersma, S. I. Bozhevolnyi, *Nat. Commun.* **2016**, *7*, 13790.

[60] F. Ding, Y. Yang, R. A. Deshpande, S. I. Bozhevolnyi, *Nanophotonics* **2018**, *7*, 1129–1156.

[61] R. F. Egerton, P. Li, M. Malac, *Micron* **2004**, *35*, 399–409.

[62] R. F. Egerton, *Microsc. Res. Tech.* **2012**, *75*, 1550–1556.

[63] D. G. Howitt, S. J. Chen, B. C. Gierhart, R. L. Smith, S. D. Collins, *J. Appl. Phys.* **2008**, *103*, 024310.

[64] M. K. Lee, T. G. Kim, W. Kim, Y. M. Sung, *J. Phys. Chem. C* **2008**, *112*, 10079–10082.

[65] S. Thomas, S. K. Nair, E. M. A. Jamal, S. H. Al-Harthi, M. R. Varma, M. R. Anantharaman, *Nanotechnol.* **2008**, *19*, 075710.

[66] Y. Chen, *Microelectron. Eng.* **2015**, *135*, 57–72.

[67] K. M. Roccapriore, M. Ziatdinov, S.-H. Cho, J. A. Hachtel, S. V. Kalinin, *Small* **2021,** 2100181.

Supporting Information

Sculpting the plasmonic responses of nanoparticles by directed electron beam irradiation

Kevin M. Roccapriore, Shin-Hum Cho, Andrew R. Lupini, Delia J. Milliron, and Sergei V. Kalinin**

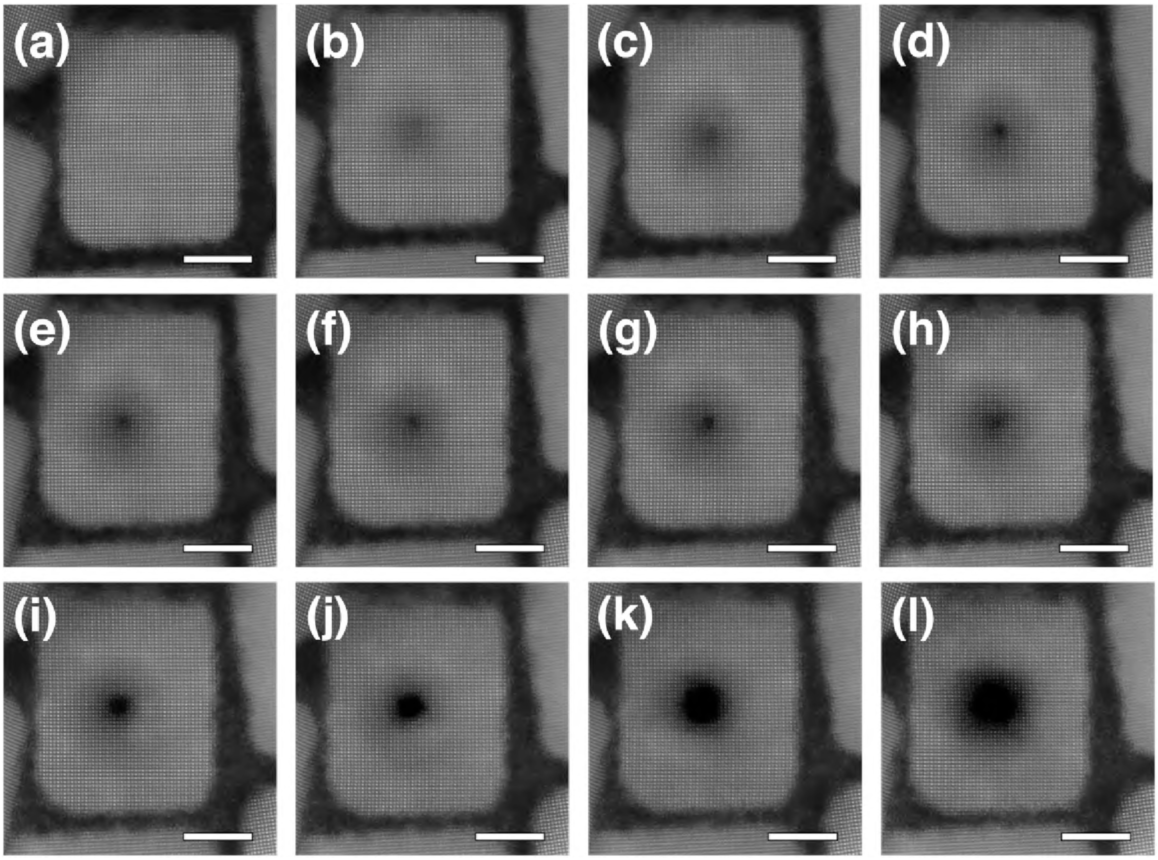

Figure S1. HAADF-STEM image time series of spot-drilling single nanoparticle. Progression of drilling in time steps of 30 seconds at reduced current compared to faster higher current drilling shown in (a-l), where atomic contrast imaging is immediately allowed following a drill step. All scale bars are 5 nm.

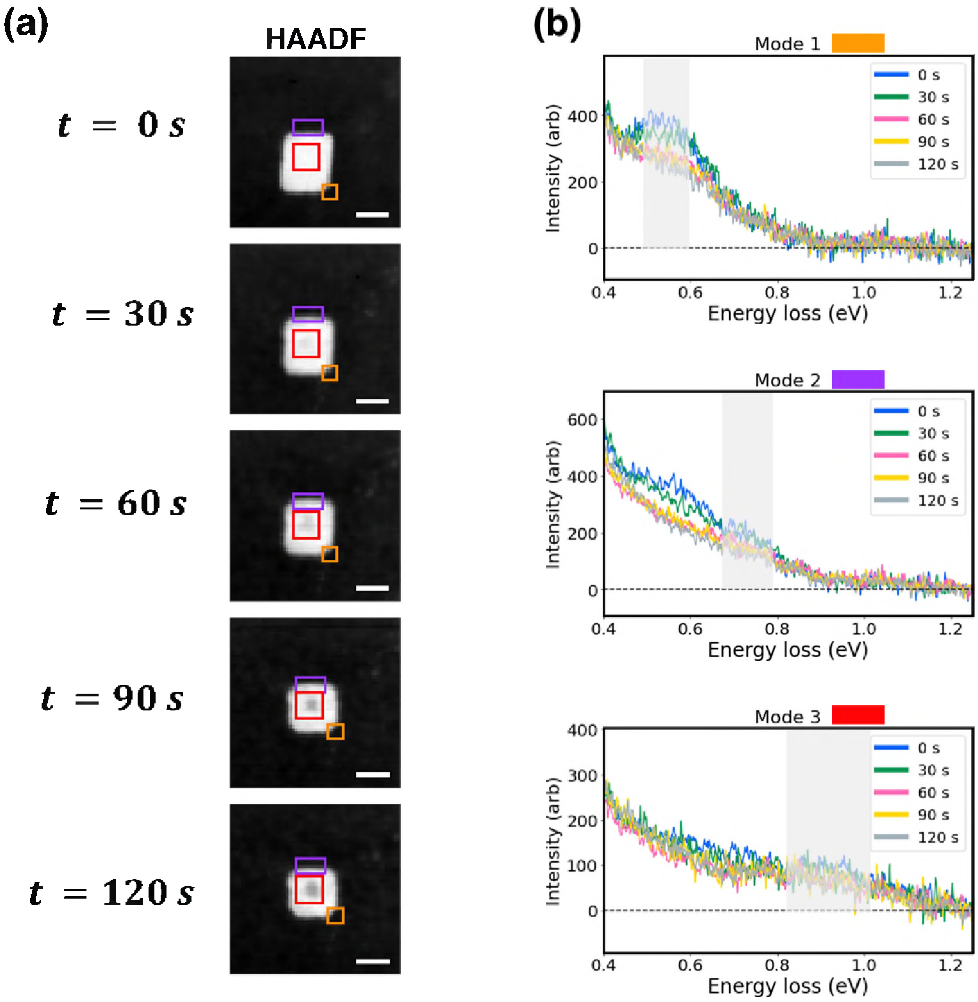

Figure S2. EEL spectra at selected ROIs near nanoparticle. (a) shows HAADF-STEM images of particle in time steps of 30 seconds while (b) shows spectra at locations shown in colored rectangles in (a) as a function of time; orange (corner) is mode 1, purple (edge) is mode 2, red (bulk) is mode 3. Transparent rectangles on (b) denote spectral region of interest for particular plasmonic feature, as multple modes can be spatially degenerate. All spectra are background subtracted to remove ZLP tails. Scale bars in (a) are 10 nm.

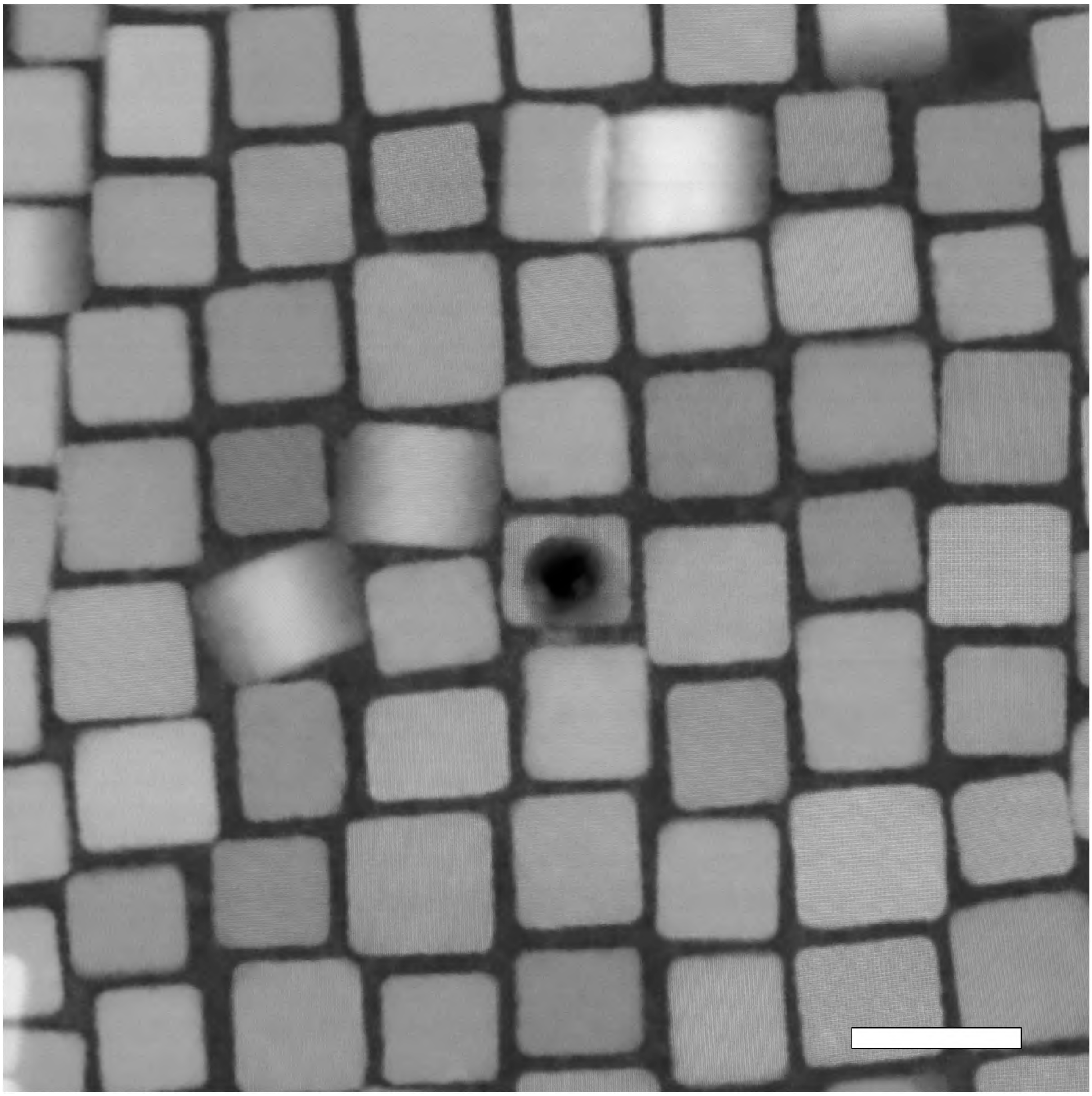

Figure S3. Preservation of crystallinity of drilled nanoparticle and nearby particles. Redeposited material is not observed on nearby particles, but is observed near bottom of drilled particle. Note that not all particles are on zone axis, therefore atomic contrast is not visible for all. Scale bar is 20 nm.

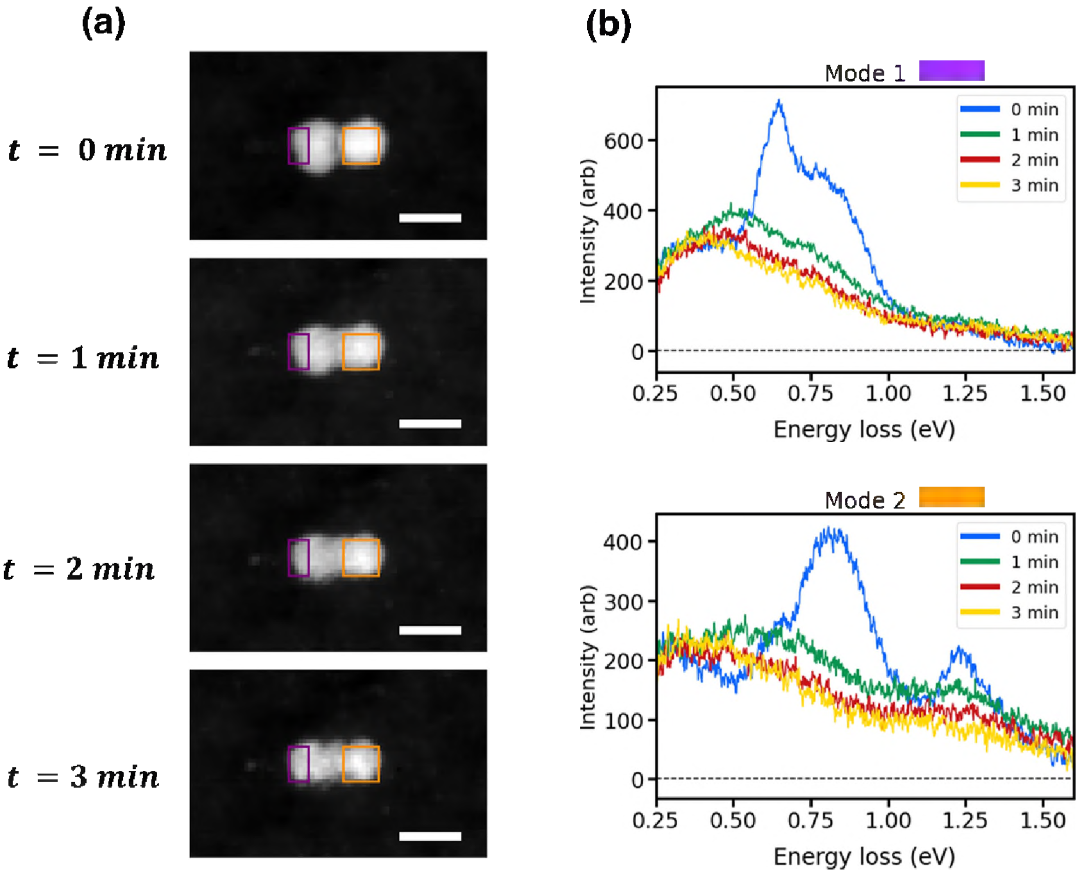

Figure S4. EEL spectra at selected ROIs near fused nanoparticle pair. (a) shows HAADF-STEM images of dimer in time steps of 1 min. while (b) shows spectra at locations shown in colored rectangles in (a) as a function of time; purple (edge) is mode 1, orange (bulk) is mode 2. Note spectra are background subtracted to remove effect of ZLP tails. Scale bars in (a) are 20 nm.

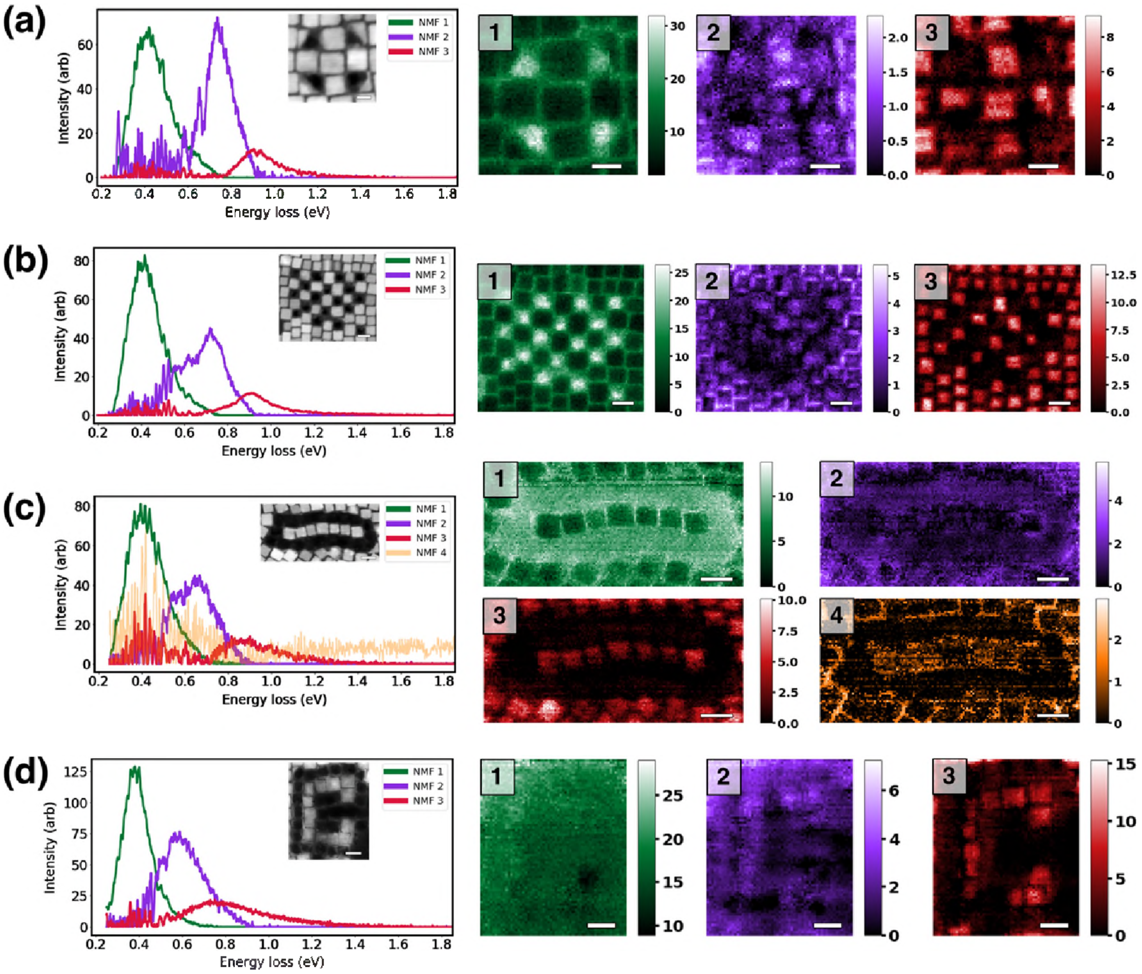

Figure S5. Additonal sculpted configurations, with NMF spectral features (left) and corresponding NMF energy maps (right). (a) diagonally cut half-nanoparticles, (b) another checkerboard with more complex periodicity, (c) One-dimensional chain of nanocubes, and (d) split-ring resonator. Note that NMF mode 3 (bulk mode) does not appear in diagonal half particles in (c), and NMF 1 in (d) is no longer localized. Due to significant material removal, there was considerable redeposition of ejected nanoparticle material and carbon contamination on (c) and (d), hence their weak spectral output. Scale bar in (a) is 10 nm, and 20 nm in (b-d).

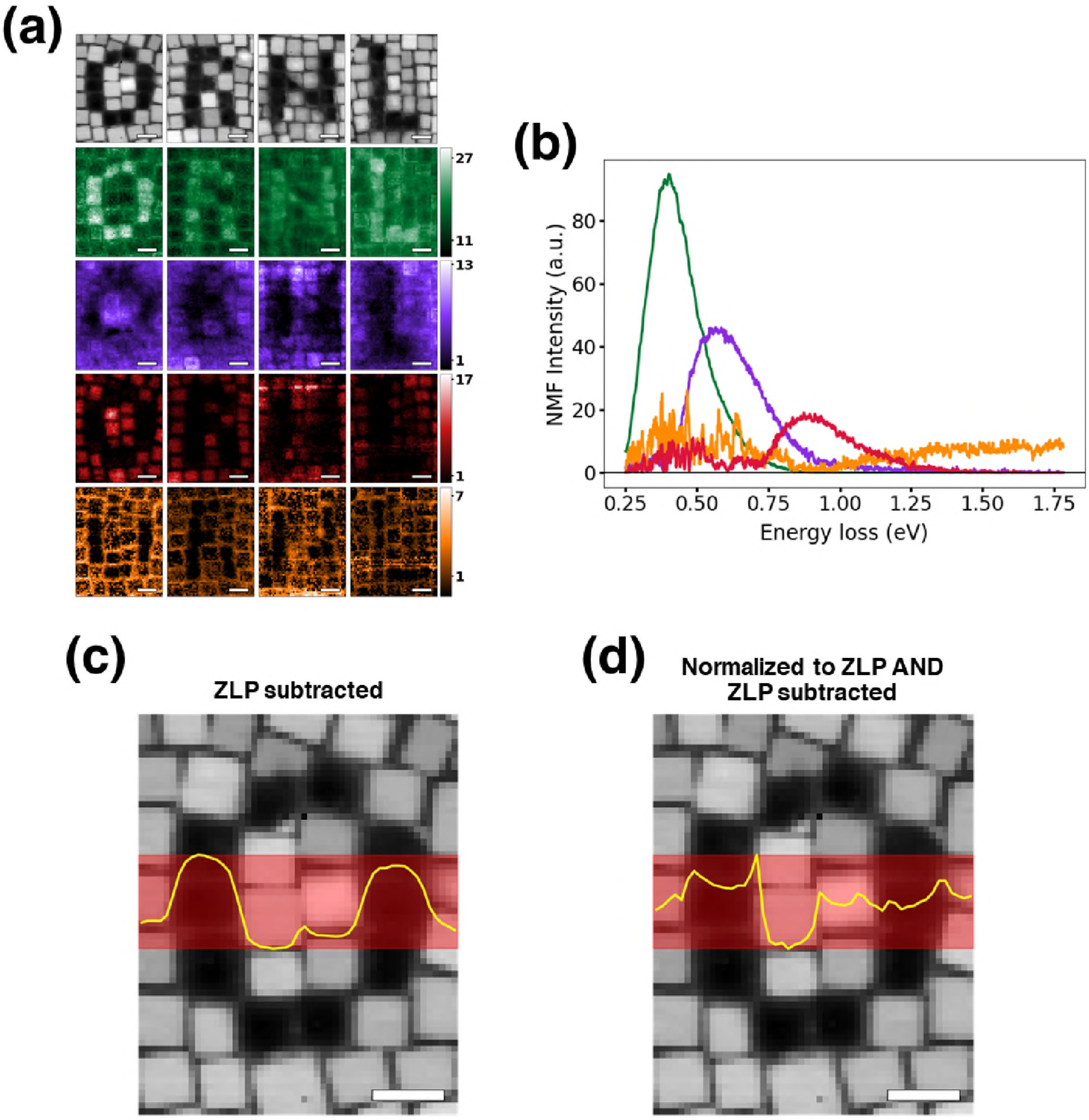

Figure S6. Effect of normaling to ZLP to account for elastic scattering. (a) NMF component maps of ORNL logo and corresponding spectral endmembers (b) after ZLP normalization. Line profiles taken across shaded regions in (c) and (d), displaying maximum pixel intensity as function of pixel position in horizontal direction. Note that possible enhancement and spatial control of plasmon intensity is qualitatively the same as shown in Figure 5. All scale bars 20 nm.

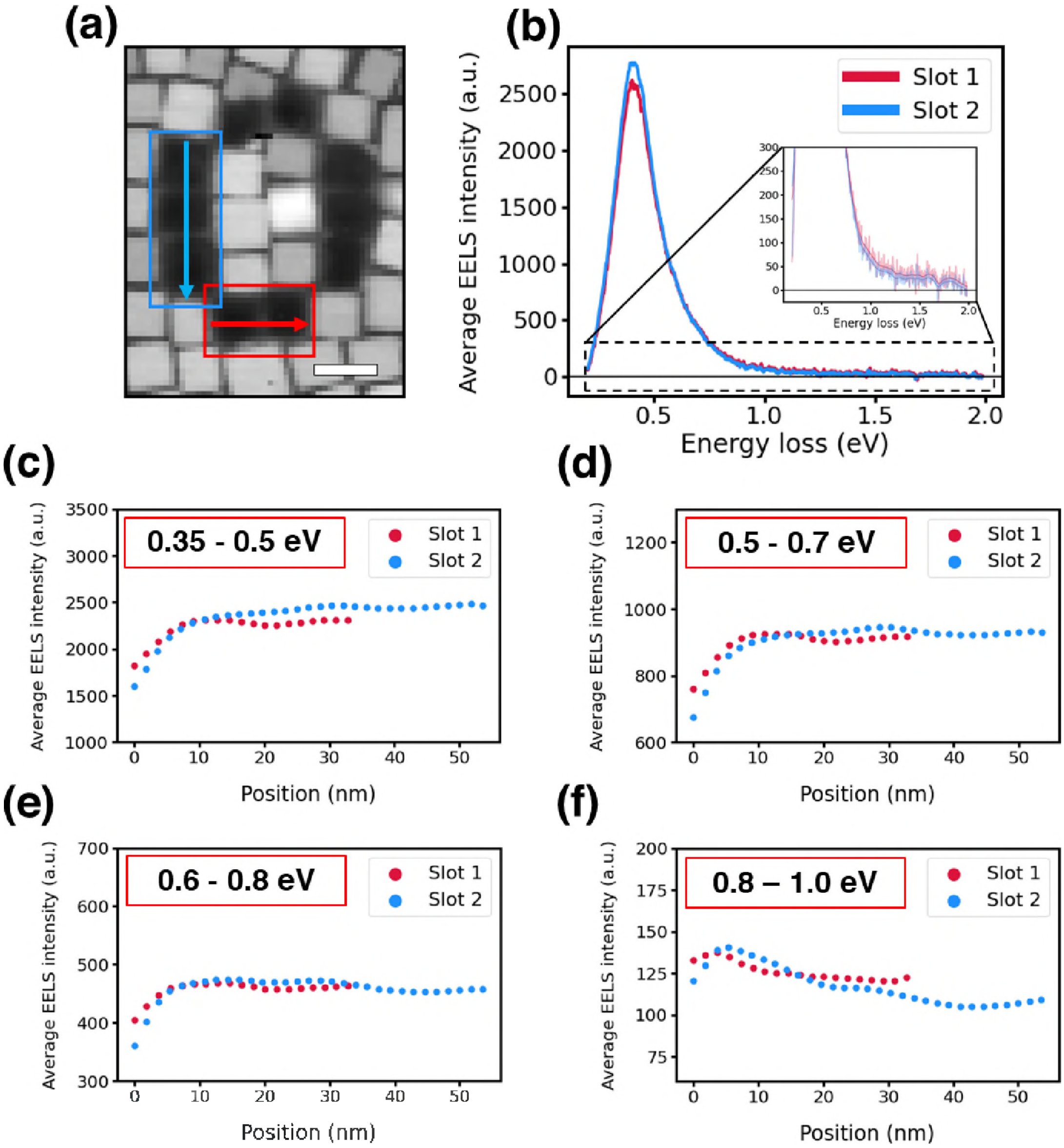

Figure S7. Slot length comparison. Two slots of different lengths are shown in (a). The energy-averaged EEL spectra is shown in (b) for each of the two slots, with inset showing an enlarged y-axis. (c-f) show position averaged EEL spectra of specified energy windows along the length of each arrow in the slot (where averaging occurs perpendicular to the arrows). Slight oscillation is correlated to the incomplete particle removal (i.e., some edges still remain) and is similar in all energy ranges. From this, existence of gap surface plasmons (GSPs) in this structure is not conclusive, largely because the particles themselves are electron transparent. Note GSPs are typically fashioned from an optically *thick* film, meaning it is not electron transparent.

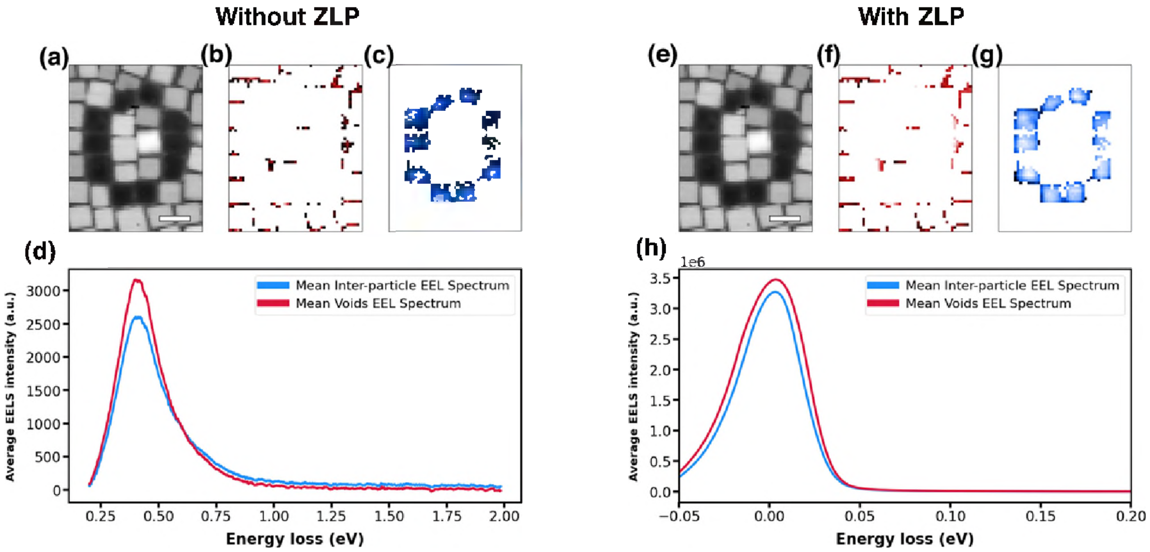

Figure S8. Spectral differences between created voids and pre-existing interparticle gaps. (a-d) show analysis of the plasmonic feature of interest (~0.4 eV), while (e-h) show elastic scattering differences through ZLP ratio. Thresholded HAADF-STEM (a,e) is used as a mask to separate gaps from voids, and the resulting energy-averaged spectrum images for masked arrays are shown in (b,c) and (f,g) for without ZLP and with ZLP, respectively. (d) and (h) are space-averaged spectrum images representing the EEL spectra from *only* the depicted regions. Scale bars in (a) and (e) 20 nm.

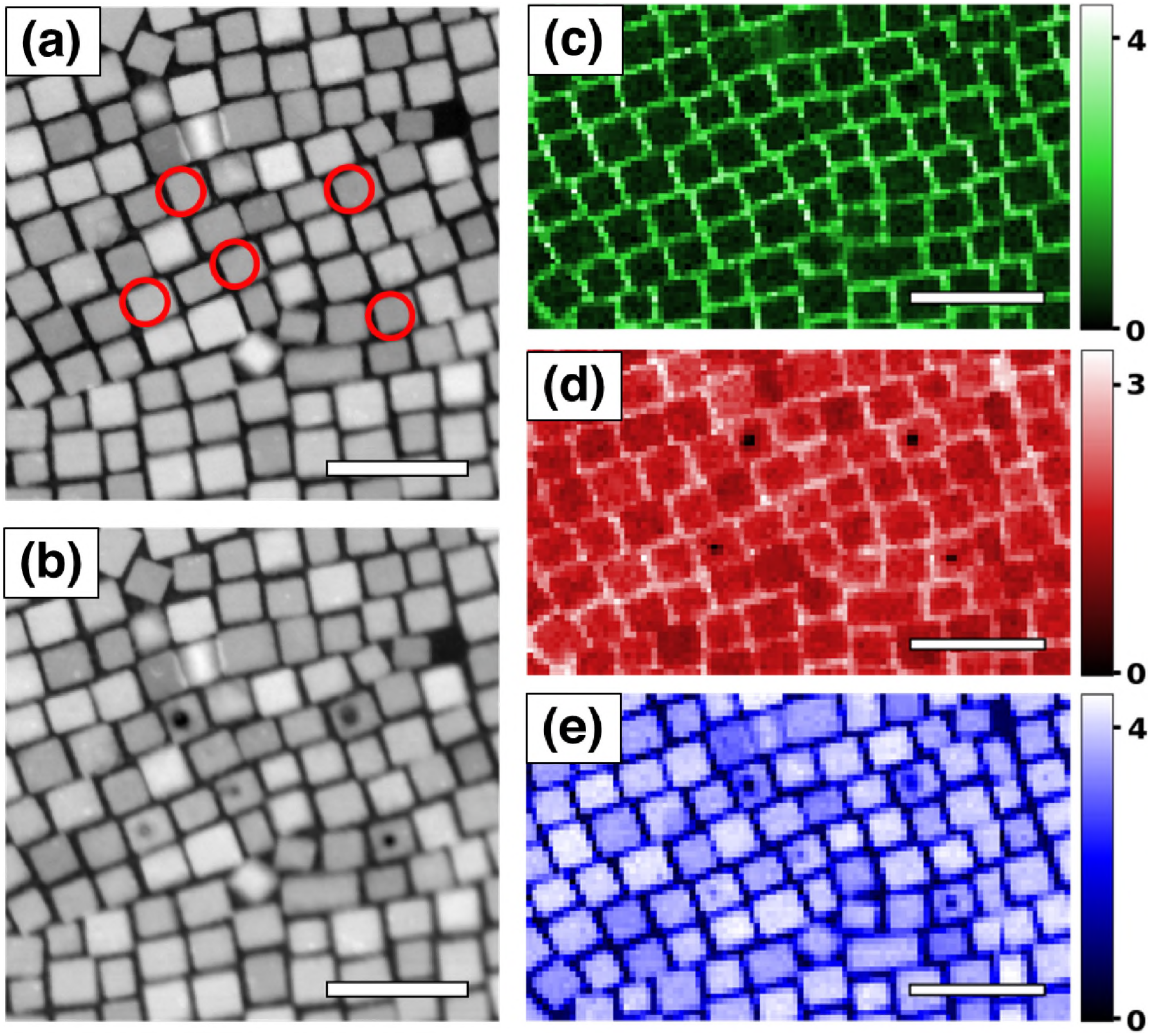

Figure S9. Chemical changes from electron irradiation. The set of HAADF-STEM images in (a) and (b) show region before and after exposure, respectively, of five different particles at varying dwell times, identified by red circles in (a). Integrated energy regions for Carbon K edge (284-334 eV), Nitrogen K edge (401-431 eV), and indium oxide (532-562 eV) features are shown in (c), (d), and (e) respectively. Chemistry of nanoparticles not intentionally exposed remains preserved. Scale bars are all 50 nm.

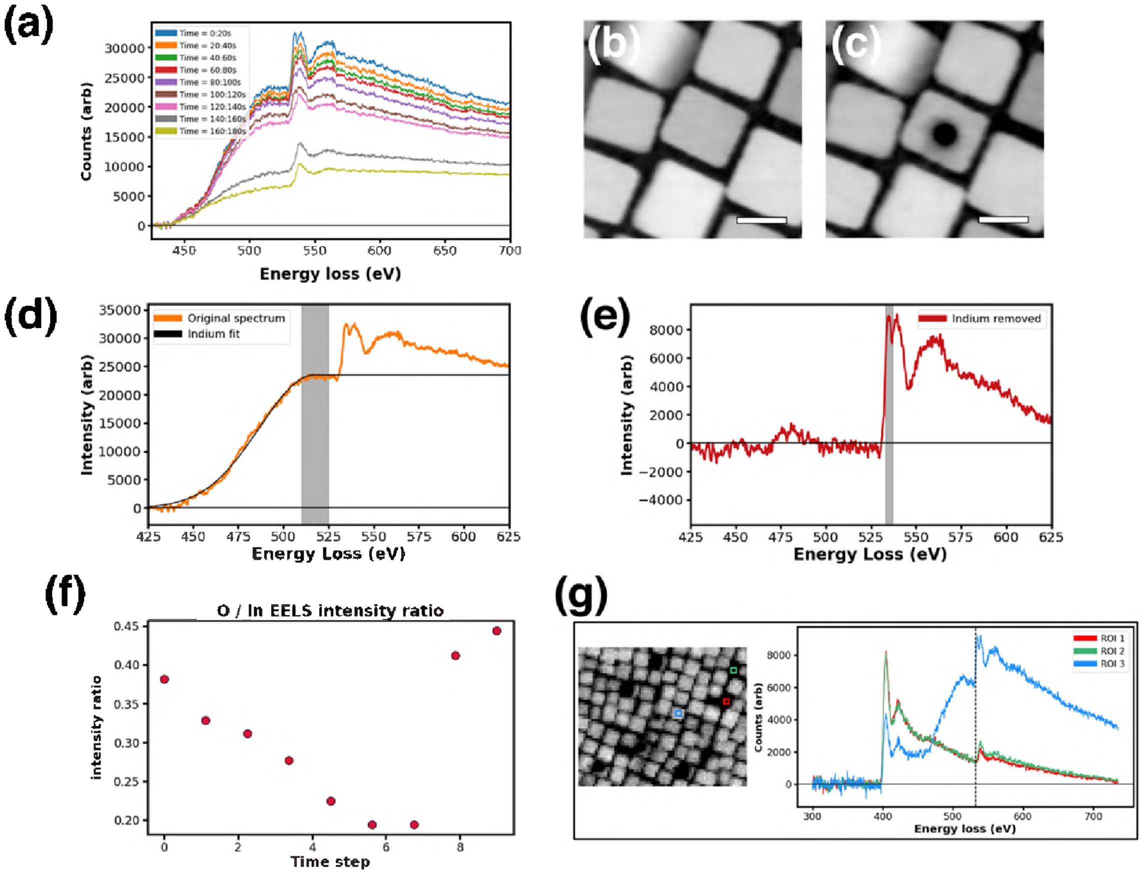

Figure S10. Time evolution of core loss EEL spectra for chemical analysis. In (a), the core-loss EELS oxygen K edge near ~532 eV in general fades in time as electron beam is fixed on particle, but the broad indium $M_{4,5}$ edge whose peak is near ~520 eV rapidly drops around 2 minutes (time step 7 to 8). This indicates preferential reduction of metallic character after a certain threshold exposure or destabilizing removal of oxygen; (b) and (c) show the HAADF-STEM images before and after irradiation. The indium $M_{4,5}$ edge is fitted with a Gaussian linearly extended from its maximum, as shown with one time step in (d) to separate the oxygen K edge intensity (e) such that a ratio of EEL edge intensities between O and In can be calculated at each time step (f). A linear extension is used instead of an exponential decay because the decay constant here depends on thickness (which changes with time), energy, etc. and is difficult to accurately extract. Gray vertical bands in (d) and (e) indicate the spectral regions where peak intensities are extracted. From the O/In intensity ratio evolution in time, it is observed that the oxygen is first removed steadily more than the indium; however, near 2 minutes of exposure, a dramatic shift occurs in which the indium is instead significantly favored to be removed. In (g), it is shown that the oxygen chemical analysis is complicated by the silicon nitride substrate that also appears to contain non-trivial amounts of oxygen (regions of interest 2 and 3 in the left HAADF), which may be attributed to oxidation, contamination, or other factors. Scale bars in (b) and (c) 10 nm.